Position Control of Parallel Active Link Suspension with Backlash

***Abstract*—In this paper, a position control scheme for the novel Parallel Active Link Suspension (PALS) with backlash is developed to enhance the vehicle ride comfort and road holding. A PALS-retrofitted quarter car test rig is adopted, with the torque flow and backlash effect on the suspension performance analyzed. An elastic linear equivalent model of the PALS-retrofitted quarter car, which bridges the actuator position and the equivalent force between the sprung and unsprung masses, is proposed and mathematically derived, with both the geometry and backlash nonlinearities compensated. A position control scheme is then synthesized, with an outer-loop H_∞ control for ride comfort and road holding enhancement and an inner-loop cascaded proportional-integral control for the reference position tracking. Experiments with the PALS-retrofitted quarter car test rig are performed over road cases of a harmonic road, a smoothed bump and frequency swept road excitation. As compared to a conventional torque control scheme, the newly proposed position control maintains the performance enhancement by the PALS, while it notably attenuates the overshoot in the actuator's speed variation, and thereby it benefits the PALS with less power demand and less suspension deflection increment.**

***Index Terms*—Active suspension, backlash, quarter car test rig, position control.**

I. Introduction

ACTIVE suspensions for road vehicles are widely studied in terms of mechatronic systems development, advanced sensors integration, intelligent control synthesis and so on [1]-[5]. The main objective pursued is the suspension performance enhancement in both ride comfort (reflected by the vertical acceleration of the car body) and road holding (reflected by the variation of the vertical tire force), while the suspension deflection should be within its maximum stroke that is permitted by the chassis mechanical structure [5]. Additionally, the energy consumption and the weight increment brought by the active components need to be evaluated to demonstrate viability of the solution for realistic automotive applications.

Parallel active suspensions are popular types, as simple retrofits can be performed to achieve suspension performance improvement with an active component that is in parallel with the spring-damper unit exerting an independent force between the sprung mass (i.e. the chassis) and unsprung mass (i.e. the road wheel). Historically, either a hydraulic cylinder or a linear electromagnetic motor is adopted as the active component due to the frequency response characteristics and the reliability of the technology [6]-[7]. In terms of control, many schemes are designed to achieve the best performance improvement with system robustness and actuator constraints respected, including linear control techniques of H_∞ and H_2 [4], [1], LQG and LQR [9], [10], and nonlinear control algorithms of sliding mode control [1], [11], [12], backstepping control [7], [13], [14], fuzzy logic [5], [15], and so on. Decent performance enhancement in ride comfort and road holding are presented in both time and frequency domain analyses.

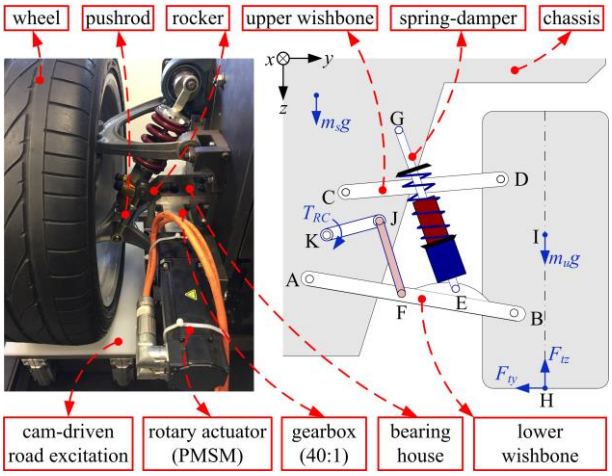

Fig. 1. Schematics of Parallel Active Link Suspension (PALS) and physical implementation (with the lower end of the pushrod, point 'F', aligned with point 'E') in a quarter car with double wishbone suspension. A PMSM (permanent magnet synchronous motor) rotary actuator is used to drive the active rocker 'K-J'. m_s and m_u are the sprung and unsprung masses, F_{ty} and F_{tz} are the lateral and vertical tire forces.

Recently, a novel Parallel Active Link Suspension (PALS) is proposed in [16], as shown in Fig. 1, where a rocker-pushrod assembly is introduced between the chassis and the lower wishbone of the suspension. This rocker is driven by a rotary actuator, which provides a torque to actively adapt to external disturbances of road irregularity and load transfer. The PALS features: 1) significant performance enhancement mainly in terms of chassis levelling and ride comfort, 2) highly limited power demand in the rocker actuation with optimized geometric arrangement of the rocker-pushrod assembly, 3) negligible unsprung mass and small sprung mass increment, and 4) fail-safe characteristics in the cases of actuator failure and power loss.

The novel PALS has been proven to be practically feasible in a quarter car experimental study, where a conventional torque control scheme is synthesized for ride comfort and road holding enhancement [17]. However, as analyzed in Section II.B in this paper, the torque control with the output of the rocker torque (T_{RC}), on one hand, simply tracks the reference value of the electromagnetic torque (assuming $T_{RC*} = G_{gbx} \cdot T_{em*}$, where G_{gbx} is the ratio of the gearbox to the rocker actuator), which can be measured by means of three-phase current (i_a, i_b and i_c) transducers and a standard d-q transformation, and therefore torque losses in the flow from T_{em} to T_{RC} are not compensated; on the other hand, the torque control introduces undesirable overshoots in the variation of the actuator speed, which is caused by the high-level backlash gap, and thereby increases

the power consumption.

Contrary to other existing control approaches for parallel active suspensions, which take the linear force or rotary torque of the active components as the manipulated control variable, in this paper, a position control scheme is designed for a PALS-retrofitted quarter car test rig, with an outer-loop H_∞ control for ride comfort and road holding enhancement and an inner-loop cascaded proportional-integral control for the reference position tracking. The main contributions are: i) the proposition of a linear equivalent model of the PALS-retrofitted quarter car, with the elasticity of the actuator transmission shaft included, ii) the novel position control scheme synthesis and implementation, which addresses the tracking inaccuracy of the desirable rocker torque due to transmission losses, and also accounts for and compensates the backlash nonlinearity in addition to suspension geometry nonlinearities, and therefore has more general applicability to active suspensions beyond the PALS, and iii) the experimental validation of the feasibility of the new position control, as well as a comparison to results with the conventional torque control.

The remainder of this paper is organized as follows. Section II introduces the PALS-retrofitted quarter car test rig, with the torque flow and the backlash effect on suspension performance discussed. Section III derives a linear equivalent model with the geometry nonlinearity compensated and transmission elasticity included. Section IV synthesizes the overall position control scheme and then implements it in the quarter car test rig. Section V performs experiments with different road profiles, and test results are compared to those with the conventional torque control. Section VI draws the conclusions.

II. PALS WITH BACKLASH

A PALS-retrofitted quarter car test rig is introduced with the torque flow and losses theoretically analyzed and the backlash effect on suspension performance experimentally evaluated.

A. PALS-retrofitted Quarter Car Test Rig

A GT (Grand Tourer) quarter car equipped with a double wishbone suspension assembly and a road excitation mechanism has been developed to experimentally study the PALS prototype [17]. Fig. 2 illustrates the schematic of the PALS-retrofitted quarter car test rig, which has two degrees of freedom and is excited by a cam-driven road mechanism: i) the sprung mass is constrained to move in the vertical direction by a carriage and railway system and therefore there is some friction (f_{rail}) in this system when the sprung mass moves, and ii) the unsprung mass is connected to the sprung mass by an actual double wishbone arrangement and therefore when there is suspension deflection the wheel moves both vertically and sideways; a Teflon road plate (the white plate in the cam-driven excitation in Fig. 1) is used to minimize the lateral friction (F_{ty}).

The PALS mechanism is integrated into the rig, with the rocker-pushrod geometry optimized to efficiently influence the vertical tire force. The low-speed shaft (LSS, i.e. the output shaft) of the actuation gearbox is connected to the rocker by a key-keyway joint, thus the backlash gap is inevitable.

A high-fidelity model of the PALS-retrofitted quarter car test rig, which has been built and validated through experimental studies, is adopted in this paper. It not only includes the theoretical model of the PALS-retrofitted quarter car, but it also takes into account the practical features existing in the rig (the

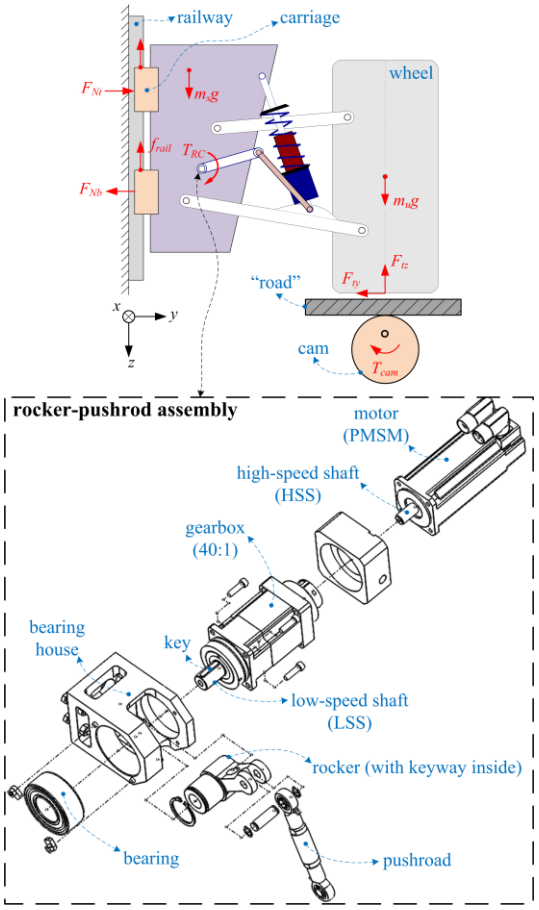

Fig. 2. Schematic of the PALS-retrofitted quarter car test rig. T_{cam} is the cam torque in the cam-follower excitation mechanism.

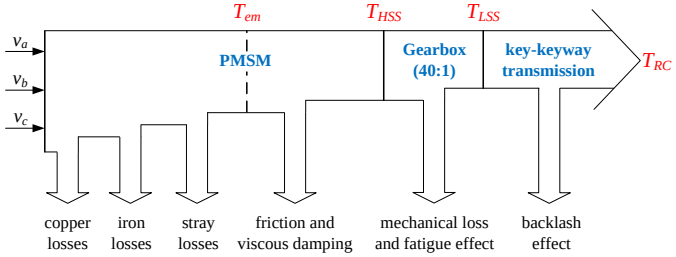

Fig. 3. Torque flow and losses in the rocker actuation, from the electromagnetic torque (T_{em}) to the rocker torque (T_{RC}).

TABLE I
MAIN PARAMETERS IN PALS-RETROFITTED QUARTER CAR TEST RIG

Parameters	Symbol	Value	Unit
Weight of sprung mass	m_s	320	kg
Weight of unsprung mass	m_u	50	kg
Spring stiffness	k_{SD}	157614	N/m
Linearized damping coefficient	c_{SD}	5792	N/(m/s)
Tire radial stiffness	k_t	275000	N/m
Tire damping coefficient	c_t	300	N/(m/s)
Rocker length	l_{RC}	74.2	mm
Pushrod length	l_{PR}	147.9	mm

sprung mass–railway friction f_{rail}, the wheel tire–road plate friction F_{ty}, and the backlash gap). The main mass properties and the geometry parameters are in accordance with an actual high-performance GT car, as listed in Table I.

B. Torque Flow and Losses

A Permanent Magnet Synchronous Motor (PMSM), which is equipped with three-phase current sensors and a quadrature encoder, is utilized to drive the rocker [18]. Due to the electrical and mechanical losses, the backlash effect and so on, there is discrepancy between the measurable electromagnetic torque of the rocker actuator (T_{em}) and the objective rocker torque (T_{RC}). The torque flow and losses in the rocker actuation (from T_{em} to T_{RC}) are illustrated in Fig. 3 and described as follows:

1) According to the standard "*d*-*q*" transformation and "zero *d*-axis current control strategy", the actuator electromagnetic torque, T_{em}, is proportional to the *q*-axis current i_q [19]:

$$T_{em} = K_e i_q, \tag{1}$$

where K_e is the torque constant.

2) The output mechanical torque of the HSS is calculated with the actuator inner mechanical losses T_M considered:

$$T_{HSS} = T_{em} - T_M = T_{em} - \left(c_r \left|\omega_{HSS}\right| + T_{rf}\right) \cdot \omega_{HSS} / \left|\omega_{HSS}\right|, \tag{2}$$

where c_r is the viscous damping coefficient, ω_{HSS} is the rotational speed of the HSS and T_{rf} is the rotor friction torque.

3) The torque conversion and loss in the gearbox stage is:

$$T_{LSS} = T_{HSS} G_{gbx} \eta_{gbx}^{M}, \tag{3}$$

where T_{LSS} is the output torque of the gearbox (in the low-speed shaft end), G_{gbx} (= 40:1) is the gearbox ratio, η_{gbx} (= 70%, nominally it is 90%) is the estimated gearbox transmission efficiency with fatigue effect taken into account, and M is the actuator operating mode (+1 corresponds to the motoring mode while -1 to the generating mode):

$$M = \left|T_{HSS}\omega_{HSS}\right| / \left(T_{HSS}\omega_{HSS}\right). \tag{4}$$

4) According to Fig. 4, the torque transmission from the input torque of the low-speed shaft (T_{LSS}) to the torque of the LSS-rocker joint (T_s) is:

$$J_m \ddot{\theta}_{LSS} = T_{LSS} - T_s, \tag{5}$$

where J_m is the motor-side inertia of the LSS, and θ_{LSS} is the angular position of the motor side.

The LSS is deemed to be elastic with material stiffness and damping, k_{LSS} and c_{LSS} (= 10 N·m/(rad/s) [21]) respectively. The torque produced in the twisted LSS is then given as:

$$T_s = k_{LSS}\theta_s + c_{LSS}\dot{\theta}_s, \tag{6}$$

where θ_s is the LSS twist angle. The LSS torsional stiffness k_{LSS} (= 3300 N·m/rad) is estimated by the LSS geometry and material properties under static conditions [17]:

$$k_{LSS} = \frac{T_s}{\theta_s} = \frac{G_{LSS} I_P}{l_{LSS}} = \frac{\pi D_{LSS}^4 G_{LSS}}{32 l_{LSS}}, \tag{7}$$

where G_{LSS} (= 79 GPa) is the shear modulus, I_P is the torsional constant of the uniform section between points 'P' and 'Q' (see Fig. 4), and l_{LSS} (= 90 mm) and D_{LSS} (= 14 mm) are the axial length and section diameter respectively of the segment between points 'P' and 'Q'.

5) Torque transmission from the torque of the LSS-rocker joint (T_s) to the torque of the load-side rocker (T_{RC}) is:

$$J_l \ddot{\theta}_{RC} = T_{RC} - T_s, \tag{8}$$

where J_l is the inertia of the load-side rocker, and θ_{RC} is the angular position of the load-side rocker.

The backlash between the actuation low-speed shaft (LSS) and the rocker is further taken into account to derive the above torques and angles. The angular positions of the motor side θ_{LSS}, of the LSS-rocker joint θ_{LSS2} and of the load side θ_{RC} are shown in Fig. 4. The LSS twist angle θ_s, the motor-load angle difference θ_d and the backlash angle θ_b (= θ_d - θ_s) are:

$$\theta_s = \theta_{LSS2} - \theta_{LSS}, \theta_b = \theta_{RC} - \theta_{LSS2}, \theta_d = \theta_{RC} - \theta_{LSS}. \tag{9}$$

As indicated by [21], the state equation of θ_b can be approximated as a limited integrator with time derivative of $\dot{\theta}_d + k_{LSS}(\theta_d - \theta_b)/c_{LSS}$ and limit α:

$$\dot{\theta}_b = \begin{cases} \max\left(0, \dot{\theta}_d + \dfrac{k_{LSS}}{c_{LSS}}(\theta_d - \theta_b)\right), & \theta_b = -\alpha \quad (T_s \le 0) \\ \dot{\theta}_d + \dfrac{k_{LSS}}{c_{LSS}}(\theta_d - \theta_b), & |\theta_b| < \alpha \quad (T_s = 0) \\ \min\left(0, \dot{\theta}_d + \dfrac{k_{LSS}}{c_{LSS}}(\theta_d - \theta_b)\right), & \theta_b = +\alpha \quad (T_s \ge 0) \end{cases} \tag{10}$$

where α (= 0.01 rad, identified through the comparison between testing and simulation results of actuator torque-speed operating points) is the half backlash gap between the LSS and the rocker.

With equations (1)-(10), the torque and angle variables in the rocker actuation can be fully defined and obtained.

The rocker torque T_{RC} is the variable that directly influences the active suspension performance, and therefore T_{RC} is conventionally taken as the manipulated control variable, based

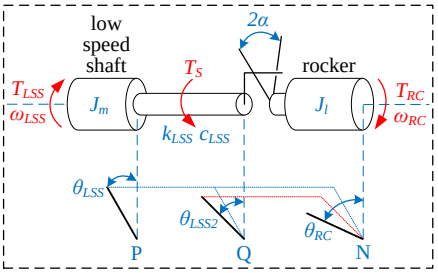

Fig. 4. Schematic of backlash in the rocker torque transmission.

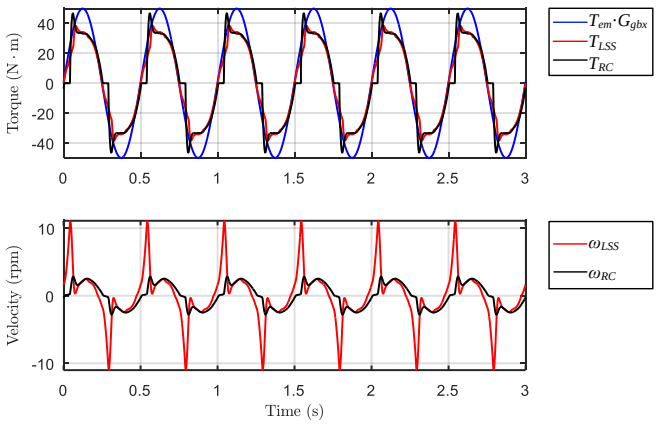

Fig. 5. Simulations of torque and speed variation in the rocker actuation and transmission, without road excitation and with a reference sinusoidal input (G_{gbx}·T_{em*}) of 2 Hz frequency and 50 N·m amplitude.

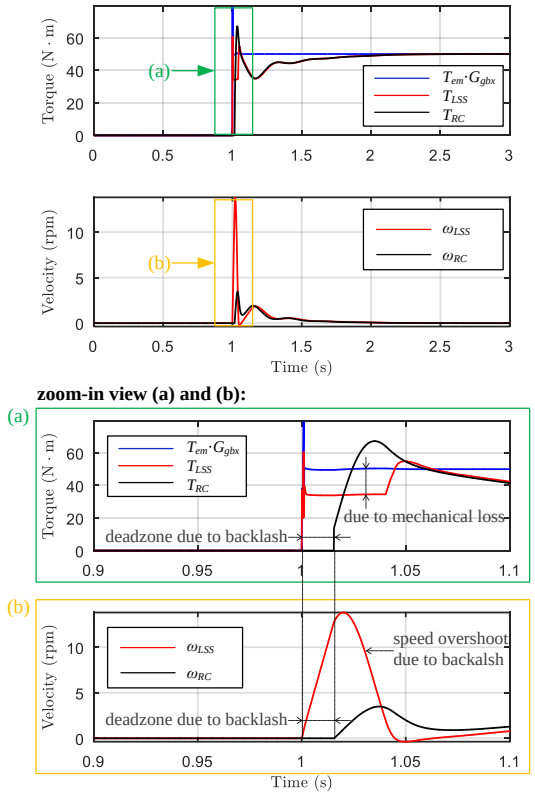

Fig. 6. Simulations of torque and speed variation in the rocker actuation and transmission, without road excitation and with a reference step input ($G_{gbx}\cdot T_{em*}$) of 0 N·m initial value (0-1 s) and 50 N·m final value (1-3 s).

on the assumption of $T_{em*} = T_{RC*}/G_{gbx}$. In order to evaluate the accuracy of this assumption, nonlinear simulations with the PALS-retrofitted quarter car test rig are performed, and the torque flow and losses, as well as the backlash effect, are analyzed. Fig. 5 shows the test rig response with a harmonic T_{em*} reference input and without any road excitation input. The peak value discrepancy between $T_{em}\cdot G_{gbx}$ and T_{RC} is mainly caused by the mechanical losses in the torque flow, while the dead zone behavior of T_{RC} variation and the overshoots in T_{RC} and ω_{LSS} variation are due to the backlash gap and clash.

Fig. 6 shows the test rig response initialized at the middle of the backlash gap ($\theta_b = 0$) with a step T_{em*} input and no road excitation, and the same conclusions can be drawn.

C. Backlash Effect on PALS Action under Road Forcing

Backlash is undesirable in torque transmission systems, as the mechanical clash and the transient changing load may accelerate the fatigue or even failure of mechanical components. With regards to the PALS system, both nonlinear simulations and experiments with a low- (α = 0.01 rad) and high- (α = 0.02 rad) level backlash gap are conducted over different road profiles, including a harmonic road, a smoothed bump and hole, and swept frequency excitation, to evaluate the backlash effect on the PALS. The low-level backlash gap corresponds to the final design adopted, while the high-level gap is imposed by a different level of manufacturing tolerance in an earlier design, and identified again through the comparison between testing and simulation results of actuator torque-speed operating points. Fig. 7 shows the experimental test results with a 2 Hz harmonic road excitation. It can be seen the backlash between the LSS and the rocker slightly affects the

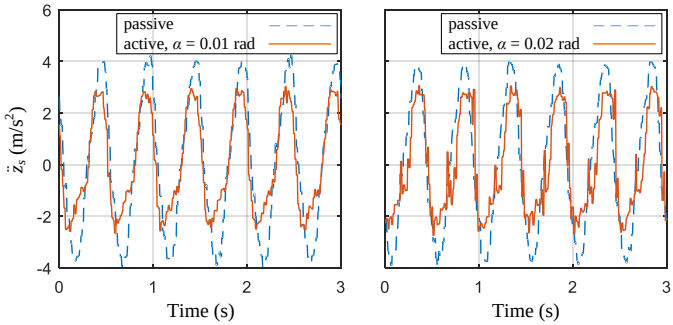

Fig. 7. Experimental test results the PALS-retrofitted quarter car test rig with a 2 Hz frequency and 2.75 cm peak-to-peak amplitude road excitation. The variable depicted above is the sprung mass vertical acceleration. A conventional torque control scheme is applied to the PALS, while a low- (left) and high- (right) level backlash gap is tested separately.

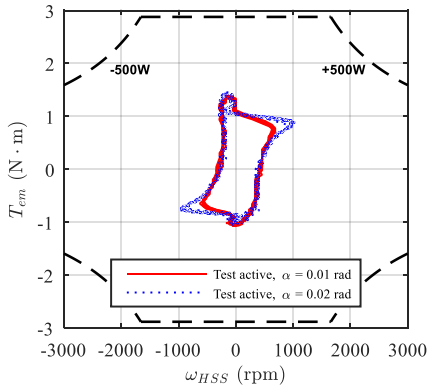

Fig. 8. Experimental test results (torque-speed operating points of the rocker actuator) of the PALS-retrofitted quarter car test rig with a 2 Hz frequency and 2.75 cm peak-to-peak amplitude road excitation. A torque control scheme is applied to the PALS, with a low- and high-level backlash gap tested separately.

active suspension performance enhancement (in ride comfort), despite spikes in the variation of sprung mass acceleration introduced by the higher level of backlash. The main negative effect of backlash on the PALS is the notable overshoots in the actuator speed variation, which results in more power consumption in the rocker actuator, as indicated in Fig. 8.

III. Elastic Linear Equivalent Model

Motivated by the torque losses and the backlash effect on the PALS, a linear control scheme with the manipulated control variable of the actuator LSS angular position (θ_{LSS}) is proposed.

As T_{RC} is the variable that directly influences the suspension performance, the relationship between T_{RC} and θ_{LSS} is expected to be derived with the elasticity of the LSS introduced.

To enable the linear control synthesis for the active suspension, a novel linear equivalent model is derived by a transformation from the nonlinear multi-body model of the test rig with backlash described in Section II. As shown in Fig. 9, 'K-J-E' is the rocker-pushrod assembly, and 'L-K-J' is the elastic low-speed shaft of the rocker actuator, which is modeled as a torsional spring with the stiffness of k_{LSS}. The angle of the rocker with respect to the horizontal plane ($\angle JKy$) is θ_{RC}, and the angle of the low-speed shaft ($\angle LKy$) is θ_{LSS}. The torque acting on the rocker from the low-speed shaft is written as:

$$T_{RC} = k_{LSS}(\theta_{LSS} - \theta_{RC}). \tag{11}$$

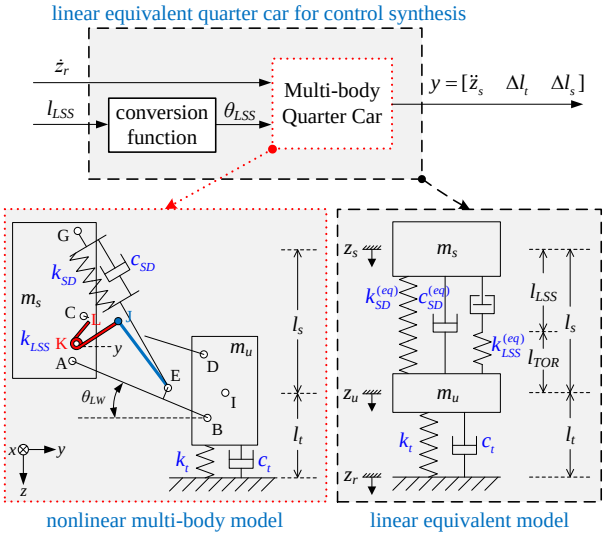

Fig. 9. Schematic of the linear equivalent model of the PALS-retrofitted quarter car with the elastic LSS. k_{SD} and c_{SD} are the spring stiffness and the linearized damping, and k_t and c_t are the tire radial stiffness and damping. Superscript (*eq*) denotes the equivalent variables. A conversion function, which is derived later in Section IV.C and given in (25), is introduced to bridge the nonlinear multi-body model (shown as the red dotted block) and the linear equivalent model (shown as the black dashed block).

In the actual multi-body model of the PALS-retrofitted quarter car, the geometry variables of θ_{RC}, l_s (the suspension deflection, defined as the vertical distance between the sprung mass center and the unsprung mass center, i.e. $l_s = z_u - z_s$,) and l_{SD} (the spring-damper length, that is the distance between points 'G' and 'E' in Fig. 9) are solely dependent on the lower wishbone angle θ_{LW}. The following derivative items that can be derived from the geometry relationship are defined and to be used in the model linearization:

$$\beta_1 = \frac{d\theta_{RC}}{d\theta_{LW}}, \beta_2 = \frac{dl_s}{d\theta_{LW}}, \beta_3 = \frac{dl_{SD}}{d\theta_{LW}}. \tag{12}$$

The following assumptions are made in the transformation from the nonlinear multi-body model to the linear equivalent model to: a) provide a simple linear quarter-car model of PALS and lumped geometric nonlinearity that preserve the essential features of the nonlinear model and are accurate for all the possible PALS actuator and suspension operation strokes, and thereby enable linear control schemes synthesis (e.g. the H-infinity control), and b) link the motor-side position (θ_{LSS}) and the load-side torque (i.e. the rocker torque, T_{RC}, which directly affects the active suspension performance) by taking into account the elasticity characteristics of the PMSM low-speed shaft (LSS):

1) Geometric equivalence: both models must have the same suspension deflection l_s and the same tire deflection ($l_t = z_r - z_u$, the vertical distance between the unsprung mass center and the road surface). Moreover, in the linear equivalent model,

$$l_s = l_{LSS} + l_{TOR}, \tag{13}$$

where l_{LSS} is the length of the linear equivalent actuator (related to θ_{LSS} as detailed later in (25)), and l_{TOR} is the linear equivalent deformation of the torsional LSS.

2) Spring-damper equivalence: the equivalent spring needs to satisfy Hooke's law, with the equivalent stiffness being:

$$\begin{aligned} k_{SD}^{(eq)} &= \frac{dF_{SD}^{(eq)}}{dl_s} = \frac{d\left(F_{SD}\cdot dl_{SD}/dl_s\right)}{dl_s} \\ &= k_{SD}(\frac{\beta_3}{\beta_2})^2 + k_{SD}(l_{SD} - l_{SD0})\frac{1}{\beta_2^2}(\frac{d\beta_3}{d\theta_{LW}} - \frac{\beta_3}{\beta_2}\frac{d\beta_2}{d\theta_{LW}}), \end{aligned} \tag{14}$$

where l_{SD0} is the length of the unloaded spring-damper unit. The equivalent damper dissipates the same energy as the actual one:

$$c_{SD}^{(eq)}(\frac{dl_s}{dt})^2 = c_{SD}(\frac{dl_{SD}}{dt})^2 \Rightarrow c_{SD}^{(eq)} = c_{SD}(\frac{\beta_3}{\beta_2})^2. \tag{15}$$

3) Torsional low-speed shaft (LSS) equivalence: by applying the virtual work principle to the system incorporating the rocker-pushrod assembly, the lower wishbone and the wheel (the sprung mass is assumed to be fixed), it yields:

$$T_{RC}\delta\theta_{RC} - F_{tz}\delta l_s = 0. \tag{16}$$

Also the linear equivalent actuator that is in series with the linear spring $k_{LSS}^{(eq)}$ exerts a vertical force F_{RC} between the sprung and unsprung masses, leading to:

$$F_{RC}\delta l_s - F_{tz}\delta l_s = 0. \tag{17}$$

Therefore,

$$\begin{aligned} &F_{RC}\delta l_s = T_{RC}\delta\theta_{RC} \\ &\Rightarrow k_{LSS}^{(eq)}(l_s - l_{LSS})\delta l_s = k_{LSS}(\theta_{LSS} - \theta_{RC})\delta\theta_{RC}, \end{aligned} \tag{18}$$

and according to the fact that the torsional LSS and the linear elastic one store the same energy, it yields:

$$\begin{aligned} &\frac{1}{2}k_{LSS}(\theta_{LSS} - \theta_{RC})^2 = \frac{1}{2}k_{LSS}^{(eq)}(l_s - l_{LSS})^2 \\ &\Rightarrow (\theta_{LSS} - \theta_{RC})/(l_s - l_{LSS}) = \sqrt{k_{LSS}^{(eq)}/k_{LSS}}. \end{aligned} \tag{19}$$

Combining (18) and (19), the linear equivalent stiffness of the torsional LSS, $k_{LSS}^{(eq)}$, is obtained:

$$k_{LSS}^{(eq)} = (\delta\theta_{RC}/\delta l_s)^2 \cdot k_{LSS} = (\beta_1/\beta_2)^2 \cdot k_{LSS}. \tag{20}$$

With further constant approximation for the derived $k_{SD}^{(eq)}$ (= 57986 N/m), $c_{SD}^{(eq)}$ (= 2029 N·s/m) and $k_{LSS}^{(eq)}$ (= 211200 N/m) at the static equilibrium state (these parameters are found to vary only slightly with θ_{LW}), the time-invariant linear equivalent model of the PALS-retrofitted quarter car is given in (21), where an external load transfer input is not included as it cannot be emulated by the quarter car test rig.

$$\begin{aligned} m_s\ddot{z}_s &= (k_{LSS}^{(eq)} + k_{SD}^{(eq)})\Delta l_s + c_{SD}^{(eq)}\Delta\dot{l}_s - k_{LSS}^{(eq)}\Delta l_{LSS} \\ m_u\ddot{z}_u &= (k_{LSS}^{(eq)} - k_{SD}^{(eq)})\Delta l_s - c_{SD}^{(eq)}\Delta\dot{l}_s + k_{LSS}^{(eq)}\Delta l_{LSS} + k_t\Delta l_t + c_t\Delta\dot{l}_t \end{aligned} \tag{21}$$

The state-space representation of the linear equivalent model is finally constructed from (21), with the state variables, outputs and inputs given respectively as follows:

$$\begin{aligned} &\hat{x}^T = \left[\dot{z}_s \quad \dot{z}_u \quad \Delta l_s \quad \Delta l_t\right], \hat{y}^T = \left[\ddot{z}_s \quad \Delta l_s \quad \Delta l_t\right], \\ &\hat{u}^T = \left[\dot{z}_r \quad (\Delta l_{LSS} - \Delta l_s)\right], \end{aligned} \tag{22}$$

where (Δl_{LSS} - Δl_s) is the manipulated control variable in the position control scheme, and the output vector $\hat{y}$ is selected with the suspension performance related variables.

IV. Position Control Synthesis

Based on the elastic linear equivalent model of the PALS-retrofitted quarter car given in Section III, a position control scheme is synthesized, with an outer-loop H_∞ control

for ride comfort and road holding enhancement and an inner-loop cascaded proportional-integral control for the reference position tracking.

The controller is then implemented into the nonlinear model of the PALS-retrofitted quarter car test rig, with the backlash nonlinearities further considered and compensated.

A. Outer-loop H_∞ Control Synthesis

The elastic linear equivalent model of the PALS-retrofitted quarter car is adopted to synthesize an H_∞ control scheme to improve ride comfort and road holding, with the manipulated control variable u being the linear equivalent deformation of the torsional LSS ($\Delta l_{TOR} = \Delta l_{LSS} - \Delta l_s$).

The configuration is shown in Fig. 10. The external disturbances, $d = [d_1\ d_2\ d_3]$, are the vertical road velocity, the measurement noise of the suspension deflection (by a potentiometer) and the measurement noise of the sprung mass vertical acceleration (by an accelerometer). The objectives to be minimized, $e = [e_1\ e_2\ e_3]$, are the weighted sprung mass vertical acceleration, tire deflection and control effort respectively.

Disturbance weighting functions [$W_{road}\ W_{d2}\ W_{d3}$] are uniform for all disturbance inputs with the DC value being the maximum possible value [20], as listed in (23), while objective weighting functions [$W_{Acc}\ W_{TD}\ W_{eff}$] penalize the importance of different objectives at specified frequency ranges [22], as listed in (24). They are tuned to mainly attenuate the performance objectives at the chassis resonant frequency (2 Hz), as well as to penalize the control effort above the frequency of interest.

$$W_{Acc} = \frac{1}{3}\cdot\frac{1}{s/(2\pi\cdot 20)+1}, W_{TD} = \frac{1}{0.003}\cdot\frac{1}{s/(2\pi\cdot 10)+1}, \quad W_{eff} = \frac{1}{350}\cdot\frac{\left[s/(2\pi\cdot 3)+1\right]^2}{\left[s/(2\pi\cdot 100)+1\right]^2}, \tag{23}$$

$$W_{road} = 0.25, W_{d2} = \frac{0.01}{(s/2\pi\cdot 5)+1}, W_{d3} = \frac{0.5}{(s/2\pi\cdot 5)+1}. \tag{24}$$

Given the sensors availability, the control feedback is selected with y_1, the suspension deflection measurement and y_2, the sprung mass vertical acceleration.

With the above selected performance objectives and these tuned weighting functions, the H_∞ controller ('K' in Fig. 10) for the elastic linear equivalent model of the PALS-retrofitted quarter car can be synthesized, while the manipulated control variable Δl_{TOR*} needs to be further converted into the reference position of the rocker actuator, $\Delta\theta_{LSS*}$, in the actual nonlinear system application. The synthesized H_∞ controller works as a bandpass filter (0.5-5 Hz) for both inputs of y_1 and y_2.

B. Inner-loop Position Tracking

As shown in Fig. 11, a cascaded position-velocity-torque control scheme is adopted to implement the reference signal tracking of the low-speed shaft position ($\Delta\theta_{LSS*}$), which is converted from Δl_{TOR*}, as detailed in (25).

In the current loop, proportional-integral controllers are synthesized to track reference q-axis current i_q and to zero d-axis current i_d (as indicated by the classic d-q transformation and zero d-axis control). The control outputs are the reference q-axis voltage v_{q*} and the d-axis voltage v_{d*}, both of which are transformed to three-phase v_{a*}, v_{b*} and v_{c*} and further feed into the PMSM servo drive. Moreover, a current clamp is added to avoid the rated or peak current being violated.

In the velocity loop, a proportional-integral controller is synthesized to zero the tracking error of the velocity of the high-speed shaft (ω_{HSS}). In addition to a speed constraint and an acceleration/deceleration constraint, a low-pass filter is introduced to i_{q*} to eliminate torque ripple caused by high-frequency signal noise.

In the position loop, a proportional controller is introduced and tuned to track the reference actuator position $\Delta\theta_{LSS*}$. All tuned parameters and added constraints are listed in Table II.

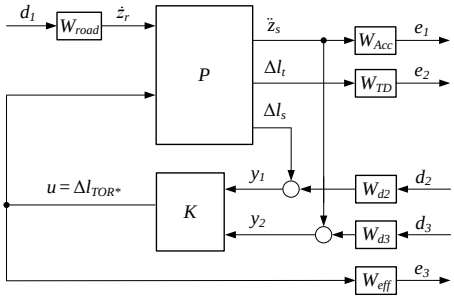

Fig. 10. Outer-loop H_∞ control synthesis with the elastic linear equivalent model of the PALS-retrofitted quarter car. P is the state-space representation of the system plant while K is the synthesized controller.

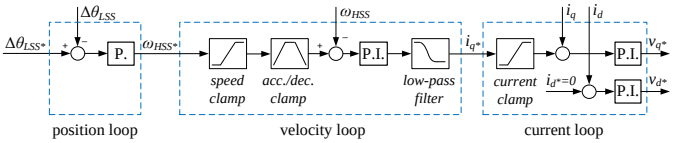

Fig. 11. Inner-loop actuator position tracking control scheme.

TABLE II
PARAMETERS OF ROCKER ACTUATOR AND SERVO DRIVE CONTROL

Parameters	Value	Unit
PMSM torque constant (K_e)	0.51	(N·m)/A
Current continous/peak limit (current loop)	5.62/7.50	A
Current proportional gain (current loop)	12.3	V/A
Current integral time (current loop)	0.725	ms
Velocity limit (velocity loop)	3000	rpm
Velocity proportional gain (velocity loop)	0.083	A/rpm
Velocity integral time (velocity loop)	6	ms
Position proportional gain (position loop)	40000	rpm/rad

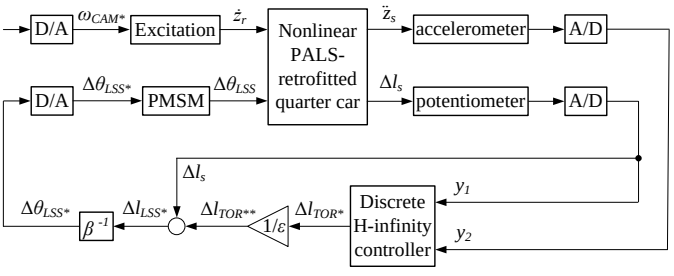

Fig. 12. Overall position control implementation to the PALS-retrofitted quarter car test rig.

C. Overall Position Control Implementation

Fig. 12 shows the overall control implementation to the nonlinear model of the PALS-retrofitted quarter car test rig.

1) The function β (in Fig. 12) not only converts $\Delta\theta_{LSS}$ in the nonlinear model to Δl_{LSS} in the linear equivalent model but also lumps the geometric nonlinearity. It is dependent on θ_{LW}, which is calculated by the measurable suspension deflection Δl_s:

$$\beta = \beta(\Delta l_s) = \Delta l_{LSS} / \Delta\theta_{LSS} = \beta_2 / \beta_1. \quad (25)$$

2) The synthesized outer-loop H_∞ controller is further discretized as the utilized real-time microcontroller has been configured with 200 Hz sampling frequency in I/O ports [23].

3) The backlash nonlinearity is further considered and compensated. As proposed in [21], a sinusoidal dual-input describing function (DIDF) is utilized to describe the backlash effect on the torque transmission:

$$\theta_d(t) = B + A\sin\omega t, \quad (26)$$

where B is a constant angle offset, and A is the amplitude of the angle variation. The output torque T_s is then approximated by a constant torque offset $N_B B$ and a first torque harmonic as below:

$$T_s(t) = T_s(\theta_d, \dot{\theta}_d) \approx N_B B + AN_A \sin(\omega t + \varphi). \quad (27)$$

In the present PALS quarter car investigation without low-frequency attitude control, no constant torque offset is applied to the elastic LSS, and the LSS damping (c_{LSS}) can be ignored for this describing function method, thus (27) is further simplified to:

$$T_s(t) \approx N_A\theta_d(t) = AN_A \sin\omega t. \quad (28)$$

Applying the above process to the backlash model given in (10), the describing functions of the elastic shaft with backlash, divided by the transfer function of the elastic shaft without backlash, can be obtained (denoted as ε) to indicate the backlash nonlinear behavior and influence:

$$\varepsilon = \frac{N_B B + AN_A \sin(\omega t + \varphi)}{B + A\sin\omega t} \Big/ \frac{}{k_{LSS} + j\omega \cdot c_{LSS}} \approx \frac{N_A}{k_{LSS}}, \quad (29)$$

where N_A, and consequently ε, is found by nonlinear simulations within the frequency range of interest to mainly depend on A/α [21] ($\varepsilon = \varepsilon(A/\alpha)$). A/α is estimated by:

$$\frac{A}{\alpha} = \frac{\max(\theta_d)}{\alpha} = \frac{\left[\max(T_{LSS}) / k_{LSS}\right] + \alpha}{\alpha}, \quad (30)$$

where T_{LSS} is approximated by $T_{LSS} = K_e \cdot i_q \cdot G_{gbx}$. Thus $\max(T_{LSS})$ is determined by the continuous/peak limits of i_q (as listed in Table II) and it is within [82, 107] N·m. With the identified α (= 0.01 rad), A/α is within [3.5, 4.2] and the corresponding value of ε is found to be [0.5, 0.7]. Therefore, the backlash effect is equivalent with shaft stiffness (k_{LSS}) attenuation without any significant introduction of phase difference.

In the position control overall implementation for the PALS-retrofitted quarter car, as shown in Fig. 12, $1/\varepsilon$ is introduced to compensate the backlash effect on the PALS.

The proposed position control scheme for the PALS-retrofitted quarter car compensates both geometry and backlash nonlinearities, and is able to zero the tracking error of the reference value of θ_{LSS*}. To validate the feasibility of the control scheme, experiments are performed with the test rig.

V. Experiments and Discussion

The PALS-retrofitted quarter car experiments with the synthesized position control scheme are performed in this section, including a harmonic road, a smoothed bump and hole, and a frequency swept road excitation. Results are compared to the PALS with a conventional torque control scheme, which employs the same H_∞ framework in Fig. 10 but with the rocker torque being the manipulated control variable and without backlash compensation.

Numerical simulation results with the nonlinear multi-body models are not presented here, as the nonlinear models have been validated to be essentially accurate and numerical simulation results can correspond to testing response.

A. Harmonic Road

The backlash effect compensator ε (in Fig. 12) in the position control scheme is experimentally tuned to be ε = 0.5 to present the best ride comfort performance within the allowance of the actuator peak current. Given the fact that the GT quarter car has a resonant frequency at 2 Hz, which is also within the human comfort interception frequencies (0-8 Hz) [22], a harmonic road of 2 Hz frequency and 2.75 cm peak-to-peak amplitude (limited by the capability of the rig excitation mechanism) is tested.

Fig. 13 shows the test results of the actual and reference signals in the inner control loop, which demonstrate that the cascaded control can accurately track the reference signals. In Fig. 14, "passive" is the case of the rocker actuator with zero torque control, which corresponds to the passive suspension. "active-t" denotes the PALS case with a conventional torque control of T_{RC}, while "active-p" is with the proposed position control scheme (with ε = 0.5). Experimental test results and comparison show that the PALS with the position control scheme maintains the suspension performance enhancement as the conventional torque control contributes, in terms of the ride comfort (sprung mass vertical acceleration). Meanwhile, the position control benefits the PALS with significant attenuation in the overshoots of the actuator speed ω_{HSS}, and thereby further reduces the variation of the suspension deflection. Moreover, as shown in Fig. 15, the position control scheme demands less power consumption in the motoring quadrants, compared with the conventional torque control.

B. Speed Bump

A speed bump is a popular road-calming device to slow on-road vehicles to improve safety conditions. A smoothed bump is tested here to further evaluate the feasibility of the position control scheme to the PALS.

The tested road profile emulates a car at constant speed of 10 km/h through a road bump with 2.75 cm in height and 1.4 m in width. According to Fig. 16, the PALS with the position control scheme contributes to the ride comfort enhancement as the conventional torque control does. Moreover, it further demonstrates that the position control scheme significantly reduces the overshoots in the variation of ω_{HSS}.

C. Frequency Sweep

A swept frequency of road excitation is conducted to evaluate the position control performance in the frequency domain, especially around the sprung mass resonant frequency (2 Hz). Test results are presented in the time domain as the road excitation frequency increases linearly form 0 to 2.5 Hz in 50 s. Suspension performance objectives of the sprung mass vertical acceleration and the suspension deflection increment are

plotted in Fig. 17 (left and middle), which shows that both the newly proposed position control and the conventional torque control can improve the ride comfort. However, due to the q-axis current (i_q) in the position control being saturated at its peak limit at higher frequencies close to 2.5 Hz, the ride comfort is slightly worse than that with the torque control. Despite the current/torque saturation, the position control notably attenuates the overshoots in ω_{HSS} variation throughout the changing frequencies, as shown in Fig. 17 (right). On the other hand, the position control demands higher torque (as the actuator has to overcome the torque losses to zero the tracking error of the reference position signal) and lower velocity, which could enable a further optimized actuator design with a gearbox of higher ratio.

Experimental results of the suspension performance improvement and the actuator power consumption with all the above road cases are further quantified and listed in Table III. As compared to the conventional torque control scheme, the proposed position control is able to maintain the level of the ride comfort improvement, and further reduces the suspension deflection variation with the actuator velocity overshoots eliminated. Moreover, the actuator uses less power (motoring) and regenerates more power, leading to a total power usage of -3.2 W against +8.3 W, respectively with the position and torque control in the 2 Hz harmonic road (the suspension with the position control is actually acting overall as an energy harvester). Finally, the peak power is 35.1W against 61.2W in the speed bump test, and 44.0W against 75.1W in the frequency sweep tests for the position and torque control respectively. Therefore, the proposed position control is more suitable for the PALS with high-level backlash.

VI. Conclusion

In this paper, a position control scheme is proposed and synthesized for the novel Parallel Active Link Suspension (PALS) with backlash, with an outer-loop H_∞ control for the quarter car ride comfort and road holding improvement and an inner-loop cascaded position-velocity-torque control for the actuator reference position tracking. Both the geometry and backlash nonlinearities are considered and compensated in the position control overall implementation. The controller is tuned to work as a bandpass filter for all inputs, and thus to make the PALS effective at human-sensitive frequencies (0.5-5 Hz).

According to test results and discussion in Section V, the position control enhances suspension performance (e.g. ride comfort) as the conventional torque control does, meanwhile it reduces overshoots in the actuator speed variation and thereby demands less power consumption. Moreover, the conventional torque control scheme for the PALS results in discrepancy between the reference rocker torque (T_{RC*}) and the actual value (T_{RC}), mainly due to the mechanical losses in the stages of the actuator and the gearbox. The proposed position control, which is based on the assumption of the transmission elasticity, is a more direct tracking of the reference actuator position ($\Delta\theta_{LSS*}$) with the internal encoders.

Despite the proposed position control scheme is sensitive to the estimation accuracy of the transmission shaft stiffness and backlash, it is found to be an alternative control approach for

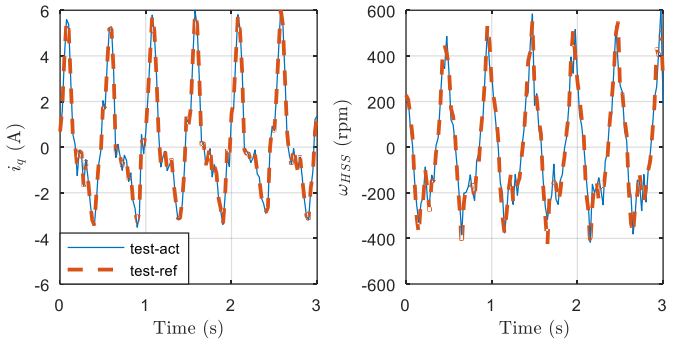

Fig. 13. Experimental test results with a harmonic road of 2 Hz frequency and 2.75 cm peak-to-peak amplitude: inner-loop reference signal tracking of i_q (left) in the current loop and ω_{HSS} (right) in the velocity loop.

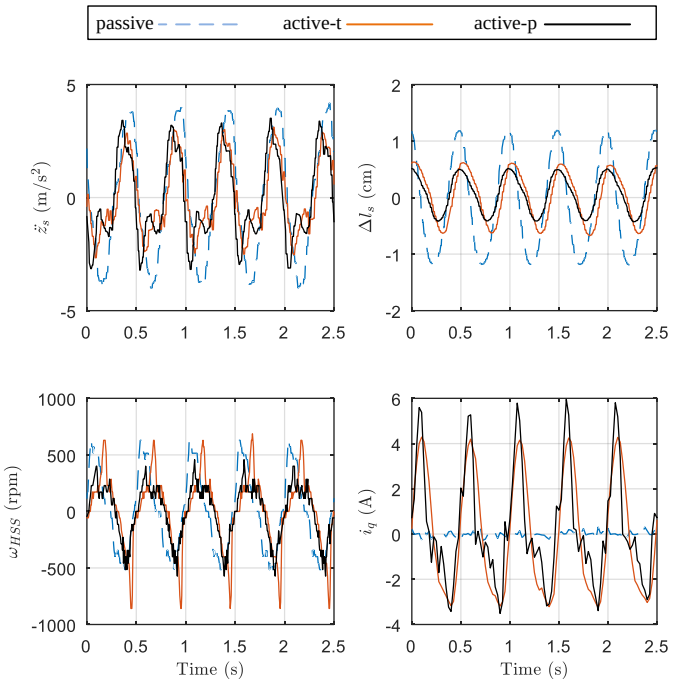

Fig. 14. Experimental test results with a harmonic road of 2 Hz frequency and 2.75 cm peak-to-peak amplitude. Variables depicted (top-left to bottom-right) are direct measurements of the sprung mass vertical acceleration (by an accelerometer), the suspension deflection increment (by a potentiometer), the velocity of the actuator high-speed shaft (by an encoder) and the q-axis current (i_q, proportional to T_{em}, and measured by current sensors).

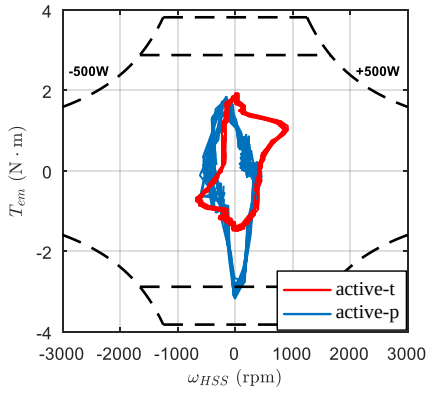

Fig. 15. Experimental test results with a harmonic road of 2 Hz frequency and 2.75 cm peak-to-peak amplitude: operation points of the rocker actuator electromagnetic torque (T_{em}) against the high-speed-shaft velocity (ω_{HSS}). The lower torque bound is the actuator rated torque while the higher one is the peak value.

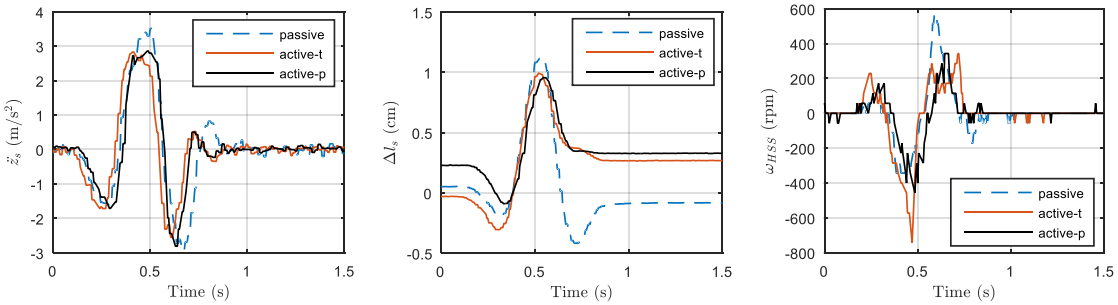

Fig. 16. Experimental test results with a smoothed bump: variables depicted (left to right) are the sprung mass vertical acceleration, the suspension deflection increment and the actuator high-speed shaft (HSS) velocity.

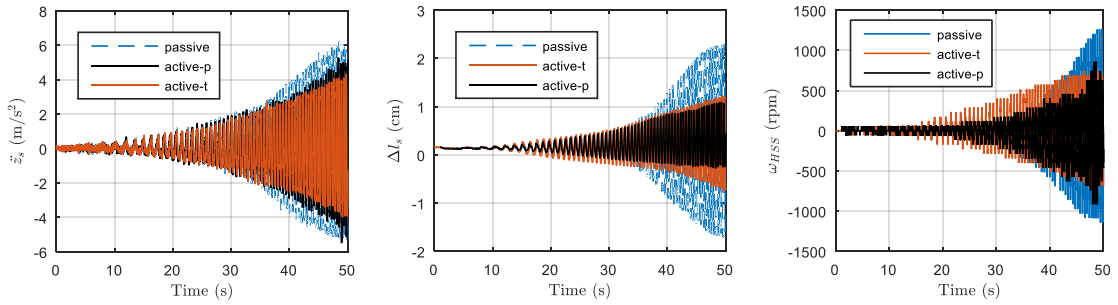

Fig. 17. Experimental test results with a frequency swept road excitation: variables depicted (left to right) are the sprung mass vertical acceleration, the suspension deflection increment and the actuator high-speed shaft (HSS) velocity.

TABLE III
EXPERIMENTAL TESTING RESULTS: COMPARISON IN PERFORMANCE IMPROVEMENT AND POWER CONSUMPTION*

Road Cases	Variables	Unit	Passive	Active-t	Active-p
2 Hz harmonic road (0-1 s in Fig. 14)	Sprung mass vertical acceleration (RMS)	m/s^2	2.70	1.89 (30.0%)	1.93 (28.5%)
	Suspension deflection variation (RMS)	mm	8.6	4.0 (53.5%)	3.6 (58.1%)
	PMSM power in motoring/generating mode/total mode (average)	W	-	+28.7/-18.1/+8.3	+9.8/-25.1/-3.2
Speed bump (0-1 s in Fig. 16)	Sprung mass vertical acceleration (RMS)	m/s^2	1.65	1.24 (24.8%)	1.37 (20.4%)
	Suspension deflection variation (RMS)	mm	4.2	3.3 (21.4%)	2.7 (35.7%)
	PMSM power in motoring mode (peak)	W	-	61.2	35.1
Swept frequency (0-50 s in Fig. 17)	Sprung mass vertical acceleration (RMS)	m/s^2	1.81	1.39 (23.2%)	1.42 (22.1%)
	Suspension deflection variation (RMS)	mm	6.0	3.2 (46.7%)	2.5 (58.3%)
	PMSM power in motoring mode (peak)	W	-	75.1	44.0

* The percentages in brackets indicate the reduction over the passive case.

the Parallel Active Link Suspension (PALS), and can even offer a control solution for general transmission mechanisms with rotary actuations, where backlash is inevitable.

REFERENCES

[1] W. Jones, "Easy ride: Bose corp. uses speaker technology to give cars adaptive suspension," *IEEE Spectrum*, vol. 42, no. 5, pp. 12-14, 2005.

[2] C. Gohrle *et al*., "Design and vehicle implementation of preview active suspension controllers," *IEEE Trans. Control Syst. Technol.*, vol. 22, no. 3, pp. 1135-1142, 2014.

[3] H. Li, J. Yu, C. Hilton and H. Liu, "Adaptive sliding-mode control for nonlinear active suspension vehicle systems using T–S fuzzy approach," *IEEE Trans. Ind. Electron.*, vol. 60, no.8, pp. 3328-3338, Aug. 2013.

[4] H. Li, X. Jing and H. R. Karimi, "Output-feedback-based H_∞ control for vehicle suspension systems with control delay," *IEEE Trans. Ind. Electron.*, vol. 61, no. 1, pp. 436-446, Jan. 2014.

[5] J. Lin and R. Lian, "Intelligent Control of Active Suspension Systems," *IEEE Trans. Ind. Electron.*, vol. 58, no. 2, pp. 618-628, Feb. 2011.

[6] T. Van der Sande *et al*, "Robust control of an electromagnetic active suspension system: simulations and measurements," *Mechatronics*, vol. 23, no. 2, pp. 204-212, 2013.

[7] W. Sun, H. Gao and B. Yao, "Adaptive robust vibration control of full-car active suspensions with electrohydraulic actuators," *IEEE Trans. Control Syst. Technol.*, vol. 21, no. 6, pp. 2417-2422, 2013.

[8] H. Chen and K. Guo, "Constrained H/sub /spl infin// control of active suspensions: an LMI approach," *IEEE Trans. Control Syst. Technol.*, vol. 13, no. 3, pp. 412-421, May 2005.

[9] M. Bégin, P. Chouinard, L. Lebel, P. Masson, Y. Pasco, J. Plante and A. Berry, "Experimental Assessment of a Controlled Slippage Magnetorheological Actuator for Active Seat Suspensions," *IEEE/ASME Trans. Mechatronics*, vol. 23, no. 4, pp. 1800-1810, Aug. 2018.

[10] H. Li, C. Tang and T. Zhang, "Controller of vehicle active suspension systems using LQG method," *2008 IEEE International Conference on Automation and Logistics*, Qingdao, 2008, pp. 401-404.

[11] B. Wang, X. Yu, and X. Li, "ZOH discretization effect on higher-order sliding-mode control systems," *IEEE Trans. Ind. Electron.*, vol. 55, no. 11, pp. 4055–4064, Nov. 2008.

[12] J. J. Rath, M. Defoort, H. R. Karimi and K. C. Veluvolu, "Output Feedback Active Suspension Control With Higher Order Terminal

Sliding Mode," *IEEE Trans. Ind. Electron.*, vol. 64, no. 2, pp. 1392-1403, Feb. 2017.

[13] N. Yagiz and Y. Hacioglu, "Backstepping control of a vehicle with active suspensions," *Control Eng. Pract.*, vol. 16, no. 12, pp. 1457–1467, Dec. 2008

[14] W. Sun, H. Pan and H. Gao, "Filter-Based Adaptive Vibration Control for Active Vehicle Suspensions with Electrohydraulic Actuators," *IEEE Trans. Veh. Technol.*, vol. 65, no. 6, pp. 4619-4626, June 2016.

[15] J. Cao, H. Liu, P. Li and D. J. Brown, "State of the Art in Vehicle Active Suspension Adaptive Control Systems Based on Intelligent Methodologies," *IEEE Trans. Intell. Transp. Syst.*, vol. 9, no. 3, pp. 392-405, Sept. 2008.

[16] M. Yu, S. A. Evangelou and D. Dini, "Control design for a quarter car test rig with parallel active link suspension," *2018 Annual American Control Conference (ACC)*, Milwaukee, WI, USA, 2018, pp. 3227-3232.

[17] M. Yu, C. Arana, S. A. Evangelou, D. Dini and G. D. Cleaver, "Parallel active link suspension: a quarter car experimental study," *IEEE/ASME Trans. Mechatronics*, vol. 23, no. 5, pp. 2066-2077, 2018.

[18] P. Pillay and R. Krishnan, "Modeling of permanent magnet motor drives," *IEEE Trans. Ind. Electron.*, vol. 35, no. 4, pp. 537-541, Nov. 1988.

[19] S. Bolognani, R. Oboe and M. Zigliotto, "Sensorless full-digital PMSM drive with EKF estimation of speed and rotor position," *IEEE Trans. Ind. Electron.*, vol. 46, no. 1, pp. 184-191, Feb 1999.

[20] K. Zhou and J. Doyle, *Essentials of robust control*. Upper Saddle River, N.J.: Prentice Hall, 1998.

[21] M. Nordin and P. Gutman, "Controlling mechanical systems with backlash—a survey," *Automatica*, vol. 38, (10), pp. 1633-1649, 2002.

[22] ISO 2631-1: 1997, "*Mechanical Vibration and Shock: Evaluation of Human Exposure to Whole-Body Vibration. Part 1, General Requirements: International Standard ISO (E)*," 1997.

[23] NI cRIO-9022 User Manual and Specifications, National Instruments, Austin, TX, USA. [Online]. Available: http://www.ni.com.